

SCIENTIFIC REPORTS



OPEN

Real-space observation of magnetic excitations and avalanche behavior in artificial quasicrystal lattices

V. Brajuskovic^{1,2}, F. Barrows^{1,3}, C. Phatak¹ & A. K. Petford-Long^{1,2}

Received: 21 June 2016
Accepted: 05 September 2016
Published: 03 October 2016

Artificial spin ice lattices have emerged as model systems for studying magnetic frustration in recent years. Most work to date has looked at periodic artificial spin ice lattices. In this paper, we observe frustration effects in quasicrystal artificial spin ice lattices that lack translational symmetry and contain vertices with different numbers of interacting elements. We find that as the lattice state changes following demagnetizing and annealing, specific vertex motifs retain low-energy configurations, which excites other motifs into higher energy configurations. Additionally, we find that unlike the magnetization reversal process for periodic artificial spin ice lattices, which occurs through 1D avalanches, quasicrystal lattices undergo reversal through a dendritic 2D avalanche mechanism.

Interactions between the localized magnetic moments on a lattice that is incompatible with the underlying crystal geometry can lead to the emergence of exotic phenomena such as spin-ice and spin-liquid phases. For example, antiferromagnetic interactions are incompatible with a triangular lattice symmetry and give rise to geometrical frustration. In geometrically-frustrated magnets, there are several degenerate ground states rather than a single stable ground state, which can lead to novel emergent phenomena and the formation of unusual magnetic excitations such as magnetic monopole defects¹. Monopole defects occur in pairs separated by Dirac strings and have been reported in a number of pyrochlore systems such as $\text{Ho}_2\text{Ti}_2\text{O}_7$ ², and Dy_2TiO_7 ³, however such phenomena are often seen only at extremely low temperatures and occur at an atomic scale, which makes them difficult to study experimentally. Model systems based on nanoscale magnetic islands or bars that act as Ising spins, patterned on various two-dimensional lattice geometries, have been realized experimentally and have been shown to exhibit similar phenomena such as monopole defects connected by Dirac strings^{4–6}. The advantage of such systems is that the large energy scale makes them easier to control, and the effects are observable at room temperature. However, so far the most common lattice geometries that have been explored have long-range periodic symmetry, for example square, triangular, and hexagonal^{4,7,8}. The combination of lattice aperiodicity with magnetic interactions can be expected to lead to further exotic excitations and the emergence of new physical phenomena.

Quasicrystals are metallic alloys that exhibit long-range order and rotational symmetry, yet possess aperiodicity. As a result, they lie between periodic crystals and disordered amorphous solids. Such long-range order along with aperiodicity modifies the electronic, vibrational and magnetic properties of the quasicrystals. In the last few years, there have been reports of long-range magnetic order as well as antiferromagnetic order observed in quasicrystals⁹. Although an increasing amount of research is being conducted on the family of local-moment bearing binary quasicrystals, there is a need for exploration of model systems to gain a deeper understanding of the magnetic interactions on an aperiodic lattice¹⁰. One of the key features of quasicrystals is the variation of coordination number from one lattice site to another. These variations lead to a different type of frustration as compared to that present in periodic or disordered lattices. In a periodic lattice, the frustration can be said to be isotropic, i.e. it affects all the lattice sites in the same way, whereas in disordered lattices, the frustration is random from each site to the next. Contrary to these cases, the frustration in quasicrystals is non-isotropic, however it is also not random due to the self-similarity of the lattice.

In order to understand the spatial effects of frustration, we need to be able to visualize the local magnetic moments and their spatial distribution, as well as get information from the ensemble lattice, particularly in response to external stimuli. Furthermore, there is interest in achieving the ground state for such magnetic interactions and understanding how deviations from it, i.e. magnetic excitations, manifest themselves. The

¹Materials Science Division, Argonne National Laboratory, 9700 South Cass Avenue, Lemont, Illinois 60439, USA.

²Department of Materials Science and Engineering, Northwestern University, 2220 Campus Drive, Evanston, Illinois 60208, USA. ³Applied Physics Program, Northwestern University, 2220 Campus Drive, Evanston, Illinois 60208, USA. Correspondence and requests for materials should be addressed to C.P. (email: cd@anl.gov)

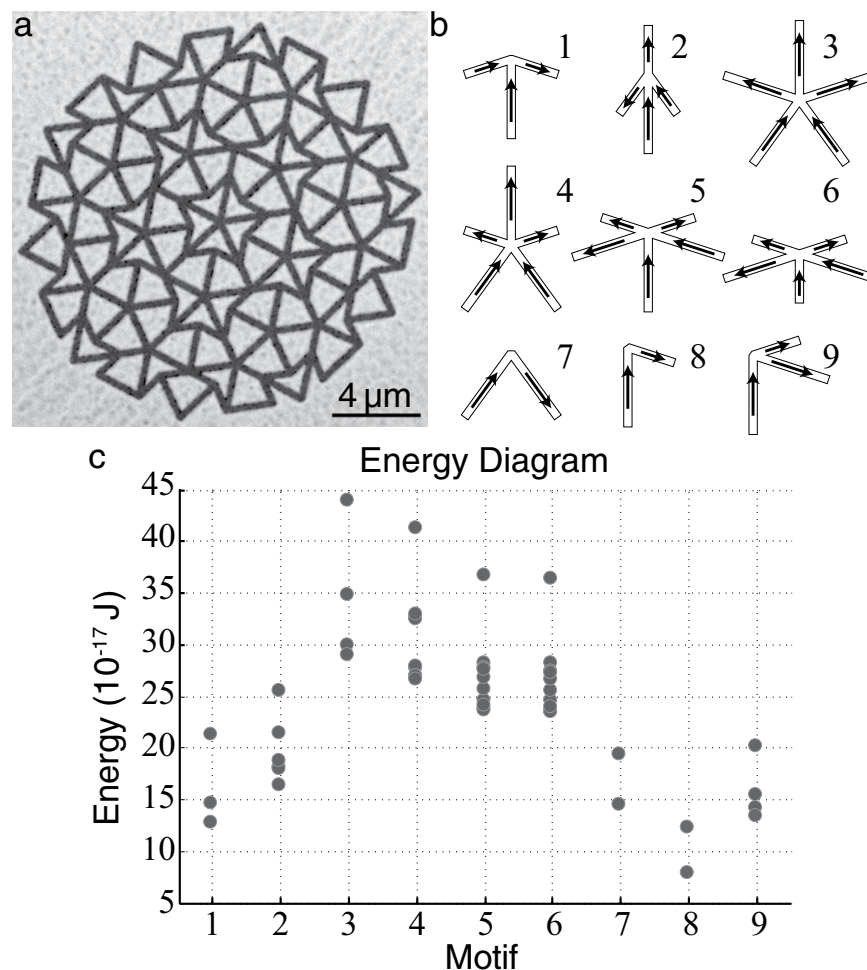


Figure 1. (a) Bright-field TEM image of QC lattice ii. (b) Schematics of the vertex motifs with arrows indicating the magnetization directions for the lowest energy states. (c) Energies of the vertex motif configurations.

aperiodicity of the QC lattice means that there cannot be a simple collinear magnetic ordered state, and previous Monte Carlo simulations on ferromagnetic Penrose tilings have shown the emergence of quasi-ferromagnetic order with ordered decagonal rings and a disordered frustrated phase inside the decagons¹¹. Similarly, Monte Carlo simulations on *antiferromagnetic* Penrose tilings have shown a fractal structure with mixed frustrated states present in the lattice¹². However, experimental realization of such effects, in addition to realization of the ground state behavior and magnetic excitations, has only recently been reported^{13,14}.

Previous work on QC artificial spin ice lattices has largely focused on FMR studies of the dynamics of magnetic reversal^{13–15}. In this work, we present analysis of the magnetic interactions, based on direct observation of a 2D quasi-crystalline (QC) artificial spin ice lattice that has been lithographically-patterned from a ferromagnetic film. The artificial QC spin ice that we explore is a P2 Penrose tiling¹³. We report on the observation of the local magnetic structure using high resolution Lorentz transmission electron microscopy (LTEM). While recent work by Bhat *et al.* has shown direct observation of as-deposited and field-cycled QC lattices using scanning electron microscopy with polarized electrons and photoemission electron microscopy, these images were viewed in a more global sense to demonstrate the presence of long-range magnetic order in QC artificial spin-ice lattices¹⁶. We instead present a novel quantitative analysis of the spatial distribution of the energy landscape across the lattice based on mapping the configurations at each individual lattice vertex, which allows us to obtain a detailed profile of the energy landscape of the QC lattices. We have analyzed the QC artificial spin ice lattice in different states, namely as-fabricated, after rotational AC demagnetizing (see Methods section)¹⁷, and after thermal annealing, to gain insights into the nature of the ground state, and to observe the magnetic excitations in the lattice. We also elucidate the dendritic avalanche mechanism by which magnetization reversal of the magnetic bars proceeds, using *in-situ* LTEM magnetizing experiments.

Energy landscape of the QC lattices

Figure 1a shows a bright-field (BF) TEM image of QC lattice ii (see Methods for details). A convenient way to analyze the QC lattices is to consider the vertices at which the magnetic bars meet. There are nine distinct vertex motifs in each QC lattice, as shown in Fig. 1b. Motifs 1–6 are found in the interior of the QC lattice, whereas motifs 7–9 occur only at the lattice edges. As can be seen in Fig. 1b, the number of magnetic bars that meet at

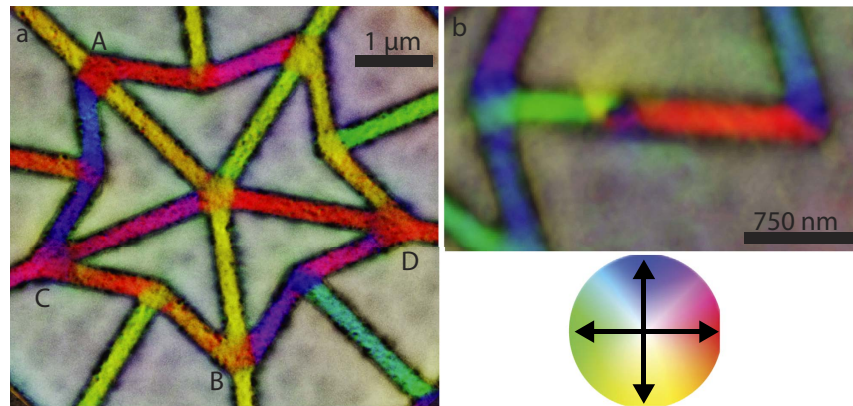


Figure 2. (a) Color magnetic induction map of the central portion of QC lattice ii. Motif-2 vertices A and B have the same configuration as each other. Vertices C and D also have the same configuration as each other. (b) Higher magnification magnetic induction map of one of the transverse domain walls seen after thermal annealing.

a vertex varies from two to five, with four distinct five-bar motifs that arise because of the different bar lengths and their spatial arrangement. Each bar can effectively be considered as an Ising spin, since the shape anisotropy confines the magnetization to lie along the length of the bar.

As the magnetization configuration changes for a given motif, so the energy of the motif changes. The energies of each vertex motif were calculated using the Object-Oriented MicroMagnetic Framework (OOMMF) software for all distinct configurations¹⁸. The arrows included on the bars in Fig. 1b show schematically the magnetization directions that correspond to the lowest energy configuration for each vertex motif. For each motif, the lowest energy configuration was the one that minimized the effective magnetic charge at the center of the vertex, with the additional condition that all bars with magnetization pointing outwards (or inwards) from the vertex are adjacent. This second condition minimizes the exchange energy at the vertex and reduces the number of domain walls that must be formed, with the associated energy cost. Figure 1c shows the calculated energies of the different magnetization configurations for each of the nine vertex motifs. The vertex motifs with fewer connected bars (1–3 and 7–9) have fewer possible magnetization configurations that are distinct in energy. The vertex motifs at which five bars come together (3–6) can take a larger number of possible magnetization configurations and, for motifs 5 and 6, the majority of these configurations have very similar energies. It should be noted that vertex motif 3 has very high symmetry and, therefore, high degeneracy for each of the low energy configurations.

A major advantage of using aberration-corrected LTEM is that we are able to obtain images of the magnetization configuration at each of the vertices with very high spatial resolution, on the order of 10 nm. Figure 2a shows a color magnetic induction map of the center of QC lattice ii in the demagnetized state. The color wheel identifies the magnetization direction in each bar as determined by transport-of-intensity equation (TIE) reconstruction (see Methods section). Motif-2 vertices labeled (A) and (B) have the same magnetization configuration, and therefore show the same domain structure around the vertex, with a domain wall separating the bar whose magnetization points in the opposite direction to that of the other three. Similarly, motif-2 vertices (C) and (D) have the same magnetization configuration and thus show the same domain structure, however in this configuration no domain walls need to form as the magnetization within all of the bars points along the same general direction. Figure 2b shows a color magnetic induction map of one of the transverse domain walls that are seen after annealing, which will be discussed in more detail later. All of the transverse domain walls that were observed show the same structure, which they adopt to lower the overall energy for bars containing head-to-head domains.

Artificial spin ice lattices are typically considered to be “athermal” systems, i.e. the magnetization is frozen in as the sample is being grown, due to their geometry and the size of the magnetic bars⁷, and it has been shown that for lattices fabricated using electron-beam lithography the deposition process can leave large areas of the as-fabricated artificial spin ice lattice in the ground state. However, the QC lattices being discussed here are distinctly different from the typical artificial spin ice lattices reported earlier^{7,19}. In the current study, we have fabricated the QC lattices using a top-down approach, i.e. the magnetic bars were patterned out from a continuous thin film using direct FIB milling^{20,21}. As a result, we can expect that the as-fabricated state in our lattices will be significantly different²², and will reflect the initial magnetization configuration in the unpatterned film, as discussed below.

In order to explore this behavior, we analyzed three different states for each of the four lattices: as-fabricated, demagnetized by rotating in a gradually-reducing alternating magnetic field²³, and finally thermally annealed by heating to 650 °C for 5 minutes followed by furnace cooling to room temperature²⁴. The reconstructed, colored magnetic-induction maps for QC lattice ii are shown in Fig. 3 for (a) the as-fabricated, (b) the AC demagnetized, and (c) the thermally-annealed states. The inset color wheel shows the direction of magnetic induction as determined by the TIE phase reconstruction. Although differences were seen between the four lattices, the same qualitative conclusions can be drawn in each case. The as-fabricated state (seen in Fig. 3a) shows an underlying anisotropy such that the magnetization in the bars tends to point as close as possible towards the blue direction,

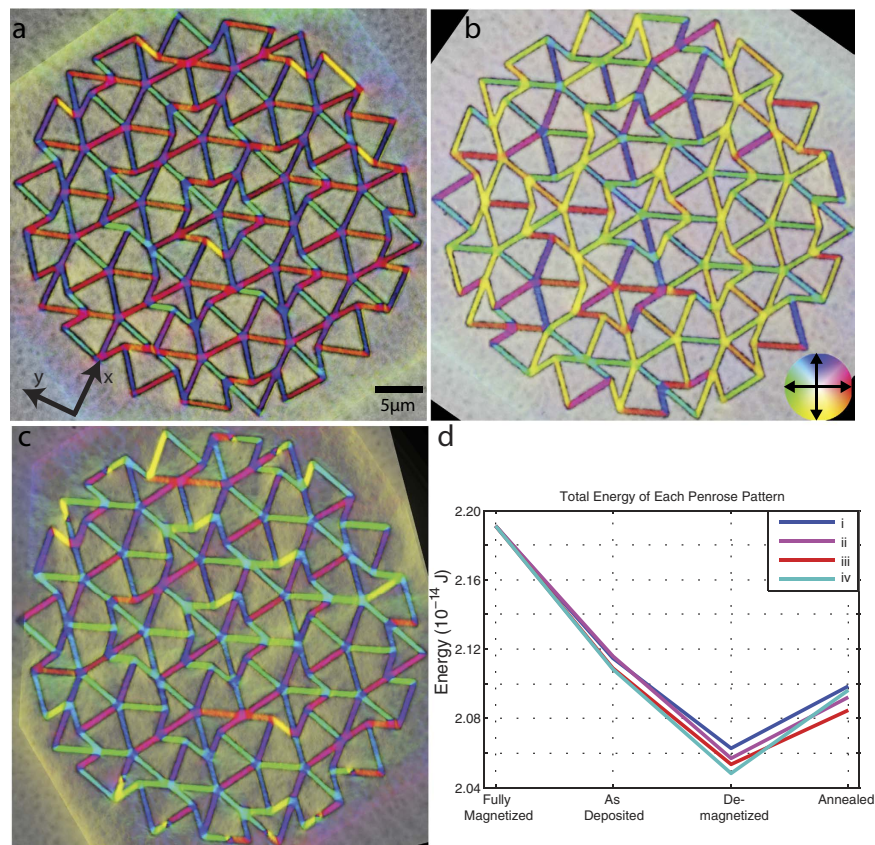


Figure 3. Color magnetic induction maps for QC lattice ii in the (a) as-fabricated, (b) demagnetized, and (c) thermally-annealed states. The magnetization direction is indicated by the color wheel. (d) Plot of total energy vs state for the four different QC lattices (i–iv). Note that the energy for the fully-magnetized state was obtained from a simulation. The black arrows in (a) show the directions used for magnetization calculations.

given the constraints of shape anisotropy. This is consistent with our observations of the Permalloy films in unpatterned windows using LTEM Fresnel contrast. This showed that the domains in the Permalloy film were much larger than the grid windows and thus the magnetization in each window before patterning was uniform. The underlying anisotropy in the as-fabricated QC lattices is likely therefore to be a result of the weak induced unidirectional anisotropy that was observed in the Permalloy film before patterning. This anisotropy disappears in the demagnetized state, as can be seen from the greater variety of colors visible in the image seen in Fig. 3b, but appears again after heat treatment (Fig. 3c). A number of transverse domain walls within the QC lattice bars are seen for the thermally-annealed state (see Fig. 2b for an example), generally within bars that are close to the edge of the lattice.

We can use the color magnetic induction maps to explore the quantitative changes in the global magnetization magnitude, $|M|$. The longer bars aligned parallel or antiparallel to the x or y direction were assigned a magnetization value of $+1$ or -1 , and the magnetization of the shorter bars was scaled relative to their length. The net magnetization of the fully magnetized lattice, in arbitrary units, is 139.2. The net magnetization for the as-deposited state is 128.7. After performing the demagnetization protocol, it decreases to 29.0, but, upon heating, goes back up to 128.7, indicating a partially aligned state. This increase in magnetization is unusual because previous experiments in which artificial spin ices were heated led to a reduction in magnetization²⁴. While some of the discrepancy may come from differences in annealing conditions (our annealing was done at 650 °C for 5 minutes as opposed to 545 °C for 15 minutes), there is a further difference, in that previous annealing experiments were carried out on artificial spin ices made up of discrete bars. One possible explanation for our observation is that since we are analyzing lattices composed of connected bars, the exchange interactions at each vertex make it energetically more favorable for the magnetization in the bars that meet at that vertex to align along a common direction. This would lead to an overall preferred magnetization direction across the whole lattice and, therefore, to an increase in net magnetization. All four partially-aligned QC lattices showed the same preferential magnetization direction (despite there being five-fold rotational symmetry in the lattices). We attribute this to an effect of FIB patterning, based on our prior work indicating that this can induce a weak anisotropy, since all lattices were patterned in the same orientation. Further work on heating QC lattices needs to be done before any definite conclusions can be made as to the nature of this increase in magnetization.

The fact that the experimental color magnetic induction maps shown in Fig. 3 allow us to determine the magnetization configuration at each vertex, means that we can also determine the vertex energies. The total energy of the QC lattice was then determined by summing the vertex energies. It should be noted that this method counts

the self-energy of each magnetic bar twice, since each bar connects two vertices and its self-energy is included in both calculations. However, the self-energy terms remain constant for each of the states we considered and therefore this is a valid method for exploring the energy *differences* between the various states. For configurations that contain a transverse domain wall, additional micromagnetic simulations of the bar containing the transverse wall and the two vertices on either side were performed. The energy of this simulation was used in place of simulations of the separate vertices. The self-energy of the bar containing the transverse domain wall was included twice in order to be consistent with the calculations for other configurations. The experimentally-determined total energy of each QC lattice in all three states is shown in Fig. 3d with a different color line for each QC lattice. Figure 3d also includes the energy of a simulated fully-magnetized lattice (2.19×10^{-14} J) for comparison with the experimental data. In all cases, the energy of the as-fabricated QC lattice is lower than that of a fully-magnetized lattice, and decreases further after demagnetizing. The average energy of as-fabricated QC lattices i–iv was calculated to be 2.11×10^{-14} J, decreasing to 2.06×10^{-14} J for the demagnetized state. For the annealing conditions that we used, the energy was observed to have increased, with the average energy being 2.09×10^{-14} J. This contrasts with previous work²⁴ that showed that thermal annealing of the QC lattices led to a state that was closer to the ground state than does demagnetization. For reference, the energy of the lattice if all of the vertices are in their lowest energy state, which may or may not be geometrically achievable, is 2.02×10^{-14} J.

In order to gain more insights into the energy changes of the QC lattices for different states, we explored the occupancy of the energy configurations for each vertex motif. Figure 4a shows an energy-occupancy plot indicating the number of vertices at each energy value for each of the nine vertex motifs. The number of vertices has been summed across all four of the QC lattices analyzed. Figure 4b shows an enlarged view of the occupancy plot for vertex motifs 4–6 so that the closely spaced energy configurations can be distinguished. The number below each data point indicates the number of vertices with that energy. After demagnetizing, the number of motif-2 vertices in the lowest energy configuration increased, and the same trend is observed for the three edge-vertex motifs (7–9). Conversely, motif-1 vertices tend to adopt configurations with higher energy after demagnetizing.

After the demagnetized QC lattices were thermally annealed, the majority of the motif-1 vertices relaxed back to their lowest energy configuration, however the number of motif-2 vertices in the excited state increased as compared to the demagnetized state. The motif 3–6 vertices, each of which connects five bars, generally remain in lower energy configurations for all states. As shown in Fig. 1c, these five-fold vertices have a number of magnetization configurations that are very similar in energy, making it easy for them to change configuration without a significant energy cost. Analysis of the edge-vertex motifs (7–9) shows that more of them relax to their lowest energy configuration as the lattices go from the as-deposited state to the demagnetized state and then from the demagnetized state to the thermally-annealed state.

We also analyzed the spatial distribution of the vertex energies as shown in Fig. 4c–e for QC lattice ii in the as-fabricated, AC demagnetized, and thermally-annealed states, respectively. Blue dots represent vertices in their lowest energy configuration and white dots represent those in their highest energy configuration, with red and yellow dots representing intermediate energies. Note that for each vertex it is only the *relative* energy between its possible configurations that is being considered. For all states, the majority of the vertices are in their lowest energy configuration. Considering only those vertices with higher energy, for the as-fabricated state, the majority of the higher-energy (excited) vertex configurations lie around the edge of the QC lattice and are relatively evenly distributed. After AC demagnetizing (Fig. 4d), there are no longer any vertices in the highest energy configuration, and the majority of the edge vertices have relaxed to a lower energy. However the energy of a few of the inner vertices has increased, giving a total of 21 vertices that are in an excited state. Heating the QC lattice leads to further relaxation of the vertices, with a reduction of the total number of excited vertices from 21 to 12. All of the non-edge vertices for which the energy increased after heating were motif-2 vertices.

An example of magnetic frustration in the QC lattices is shown by the trend for the energy of motif-1 vertices to increase during the demagnetization process, and for the energy of motif-2 vertices to increase after thermal annealing. This occurs in order to allow surrounding vertices to adopt a lower energy configuration and thus lower the overall lattice energy. Conversely, motif-5 vertices are typically in a higher-energy configuration, regardless of the lattice state, again as a result of interactions with other vertices. The majority of the excited vertices occur towards the outer edges of the QC lattice, suggesting that the frustration effects accumulate at the lattice edges as having the edge vertices in an excited state has a minimal effect on the total energy.

The transverse domain walls that are observed after heating are of significant interest. At the length scale of the bars in the lattice, an individual single-domain bar has a lower energy than if it contains a transverse wall. However, when we take into consideration the energy of the vertices at either end, micromagnetic simulations showed that putting the bar in a single-domain state resulted in one of the two vertices at the end of the bar adopting a configuration with a higher overall energy. As a result, in order to expel the transverse wall, the magnetization would have to reverse in multiple bars. This suggests that the transverse walls are a transitional state that is frozen in as the QC lattice cools down. Pinning of the transverse walls during magnetization reversal, possibly as a result of crystalline defects within the bar, could also contribute to their presence.

As discussed above, the most obvious difference between the previous and current works is that the bars in our QC lattices are connected rather than being discrete islands. Another possibility is that, since the demagnetization protocol involves rotation, the increased rotational symmetry of the QC lattice allows for a more effective demagnetization process than in the square artificial spin ice lattices, as evidenced by the reduction in net magnetization to 25% of $|M|_{\max}$. Additional studies on the effect of various parameters such as annealing time and temperature, for example to determine the critical blocking temperature, are required before a heating protocol can be more effectively used to attain the minimum energy state.

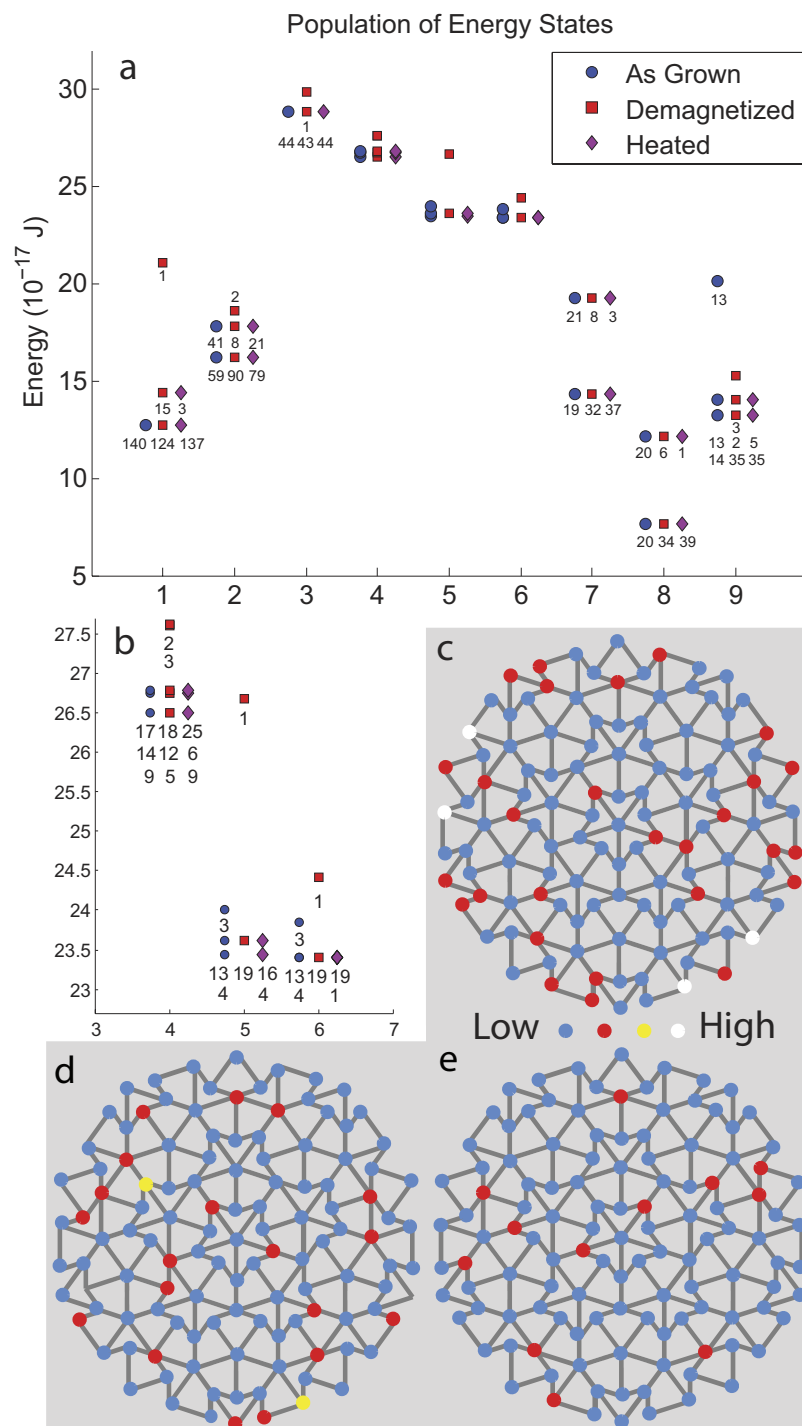


Figure 4. (a) Plot of vertex energy occupancy for each state (the numbers of vertices are summed across all four QC lattices). (b) An enlarged view of the energy occupancy for vertex motifs 4–6. (c–e) Spatial distribution of higher energy states of vertex motifs for QC lattice ii in the (c) as-grown, (d) demagnetized, and (e) thermally-annealed states.

Magnetization reversal process

In addition to exploring the change in energy following demagnetizing and thermal annealing, it is of interest to explore the process by which magnetization reversal occurs across the QC lattice during application of an external field. Figure 5a shows a schematic of the experimental magnetization reversal of the QC lattice: the color of each bar indicates the applied field value at which its magnetization direction reversed (the field-value color key is shown at the right-hand side of the schematic), and the colored arrow on each bar indicates the final magnetization direction. The magnetization of the grey bars did not reverse over the visible applied field range. The large black arrow indicates the applied field direction. The first bars to reverse their magnetization (purple/blue colors)

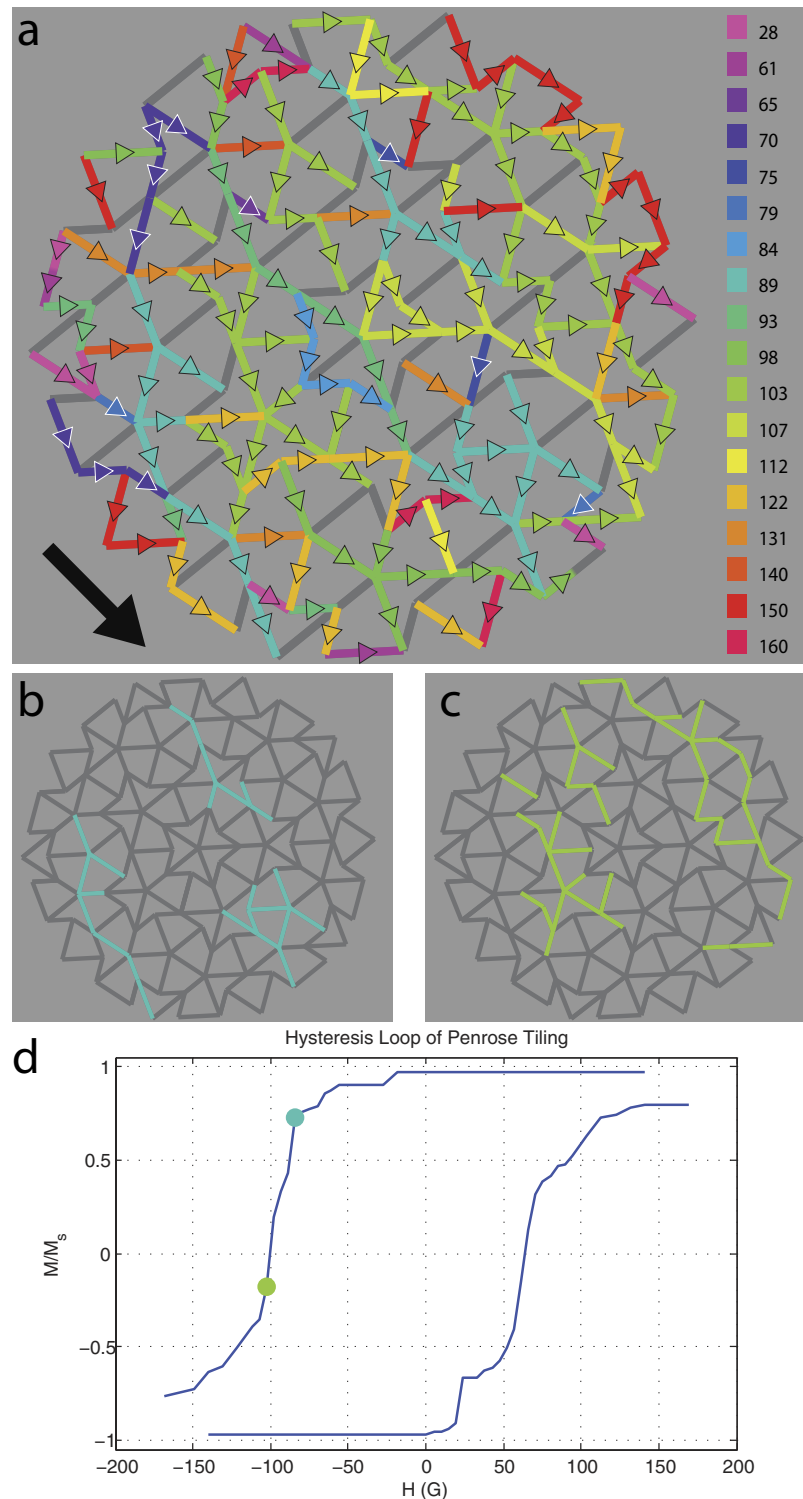


Figure 5. (a) Schematic created from Fresnel mode LTEM images, illustrating the magnetization reversal of QC lattice v . The bar color indicates the applied field value at which the magnetization in the bar reversed (see key at RH side) and the arrow shows the final magnetization direction. Large black arrow indicates applied field direction. (b,c) Schematics highlighting the dendritic cascades that occurs at 89 G and at 103 G. (d) Hysteresis loop for QC lattice v along the field direction shown in (a) (Loop reconstructed from the LTEM images). The blue and green dots show the locations of the cascades in (b,c), respectively, on the hysteresis loop.

are isolated and lie near the edges of the lattice. As the applied field increases, localized clusters of bars reverse their magnetization via a dendritic avalanche mechanism, with each avalanche spreading out from the end of a

previously reversed bar. Examples of individual cascades that formed at 89 G and at 103 G are shown in Fig. 5b,c respectively. The formation of dendritic cascades can be attributed to the lack of translational symmetry and to geometric frustration within the QC lattice, which does not allow for a more orderly growth of Dirac strings via 1D avalanches that is observed in periodic artificial spin ice lattices⁴.

The majority of the bars that are perpendicular to the applied field do not reverse their magnetization at fields low enough to be observed in the LTEM experiment, and this provides an energy barrier that can prevent the magnetization in adjacent non-perpendicular bars from reversing. The exception to this occurred in motif-1 vertices in which magnetization reversal of a perpendicular bar is required to prevent formation of the highest energy configuration (all three bars with magnetization pointing towards, or away from, the vertex). Notably, the motif-3 vertices, for which the high rotational symmetry allows a number of degenerate lowest energy configurations, were seen to maintain one of these degenerate configurations throughout the magnetization reversal via a number of bars reversing simultaneously.

An experimental hysteresis loop for the QC lattice seen in Fig. 5a is shown in Fig. 5b. The loop was reconstructed from the LTEM images. The net magnetization along the field direction was determined in a similar manner to that discussed in the previous Section to calculate the net magnetization for QC lattices i–iv, and an **M-H** hysteresis loop along the applied field direction could then be determined. The offset of the hysteresis loop by 25 G along the *x*-axis arises because of a residual field in the magnetizing holder. Accounting for this offset, the coercive field of the QC lattice is on the order of 80 G. The jumps in the hysteresis loop occur because the magnetization changes by relatively large steps as the magnetization direction in large clusters of bars reverses. These jumps in the hysteresis loops are equivalent to the “knees” seen in previous experimental observations of the hysteresis loop in QC lattices^{13,25}.

Discussion

We have observed significant differences in the behavior of our QC spin ice lattices, with respect to that of periodic lattices, due to the lattice aperiodicity. The non-isotropic nature of the frustration in a QC lattice means that different vertex motifs behave differently: all motif-3 vertices tend to remain in their lowest energy configuration, with the associated frustration being accommodated by exciting the motif-1 and motif-2 vertices into high energy configurations. This is not only observed during AC field demagnetizing and thermal protocols, but also during the magnetization reversal process.

Although QC lattices lack translational symmetry, they possess high rotational symmetry, and as a result, the rotational demagnetizing protocol achieves the state that is closest to the ground state. In the lattices with lowest energy, we observe locally-ordered regions at motif-3 vertices, along with presence of a frustrated phase at the remaining vertex motifs. This is similar to the results obtained using simulations on ferromagnetic P3 Penrose tilings¹². It is also interesting to note that the QC lattices have a very large number of degenerate ground states, mainly as a result of the degeneracy of the lowest energy for the five-fold vertices, as shown in Fig. 1. The non-isotropic frustration in these lattices accounts for the presence of the transverse domain walls that are frozen into the system upon cooling, because their removal would require a local increase in energy that is too high to be achieved. It is likely that QC lattices, having non-isotropic frustration and a lack of translational symmetry are more prone to having these domain walls frozen in than periodic artificial spin ice lattices.

The aperiodicity also affects the magnetization reversal process of the entire lattice. We can correlate the jumps or “knees” in the hysteresis curve with simultaneous reversal of clusters of bars via a dendritic avalanche mechanism that we attribute to the variation in coordination number between vertices. This is a striking difference as compared to periodic 2D lattices where typically a 1-D avalanche-like reversal behavior is observed. Further modeling of the reversal of such lattices is required to understand the role of disorder. Such information can be very useful for understanding the behavior of low temperature spin glasses and nematic liquids, which show minor hysteresis loops due to disorder.

Our work has shown the importance of being able to visualize, *in-situ*, the local magnetization configuration in QC artificial spin ice lattices. Through direct visualization of the magnetic induction, we were able to calculate a configuration-based energy for the QC lattices that allowed us to explore their energy landscape under different conditions, to spatially resolve the vertex configurations that led to the changes in energy landscape, and to observe a novel magnetization reversal process.

Methods

Four identical P2 Penrose-tiled quasicrystalline artificial spin ice lattices (QC lattices) were patterned via focused ion-beam (FIB) milling from a 20 nm thick Permalloy thin film deposited using sputter deposition onto the Si₃N₄ membrane of a Si TEM chip. We designate the lattices by i, ii, iii, and iv. The QC lattices are formed from a combination of kite and dart shapes, and this leads to the lattice being composed of two different magnetic bar lengths. The QC lattices were patterned so that the longer bars had a length of 2.03 μm and the shorter bars had a length of 1.13 μm. The width of all bars was 280 nm. The magnetization of the lattices was analyzed using LTEM with the sample sitting in a field-free region²⁶. In order to reconstruct maps of the in-plane magnetic induction from the phase shift of the incident electrons, through-focus series consisting of at least nine BF TEM images were recorded with a defocus step of Δf = 270 μm. The transport-of-intensity equation (TIE) was used to obtain the phase of the electron beam²⁷. The magnetic induction in the sample was then determined from the gradient of the phase (assuming uniform thickness of the sample) according to the equation:

$$\nabla\phi = B_{\perp}t\frac{e}{\hbar}$$

The direction of the resulting magnetic induction is indicated via a color wheel.

Demagnetizing was carried out by rotating the sample in a decreasing AC magnetic field, following a similar protocol to that developed by Ke *et al.*¹⁷. The sample was rotated at 1000 RPM, the maximum field applied was 1000 G, and the field was decreased at a rate of 3.5 G per step, with each step being held for 1000 ms. These parameters were chosen based on our previous work to demagnetize square spin ice lattices²⁸. Thermal annealing was carried out by heating the QC lattices in a sputter deposition chamber to 650 °C under vacuum and leaving them at temperature for 5 minutes before cooling. The heating source was an infra-red lamp and the lattices were positioned at least 45 cm away from the magnetron sputter target so as to prevent exposure to its magnetic field.

Simulations to calculate the energy of the various configurations for each vertex motif were carried out using the OOMMF software¹⁸. The simulation parameters that were used are as follows: the exchange constant used was $A = 1.3 \times 10^{-11} \text{ J} \cdot \text{m}^{-1}$, the anisotropy constant used was $K = 0$, and the saturation magnetization was $M_s = 8.6 \times 10^5 \text{ A} \cdot \text{m}^{-1}$. The total size of the simulation was $4.5 \mu\text{m} \times 4.5 \mu\text{m} \times 20 \text{ nm}$, with a cell size of $5 \text{ nm} \times 5 \text{ nm} \times 5 \text{ nm}$. The initial configuration was determined from a bitmap, and the simulation was allowed to relax using a conjugate-gradient evolver.

We also carried out *in-situ* LTEM magnetizing experiments to understand the magnetization reversal process in the QC lattices. The configuration of our magnetizing holder required that a separate QC lattice be patterned from the same thickness of Permalloy film onto the Si_3N_4 membrane window on a 2 mm TEM Si chip. A slightly different P2 Penrose tiling, referred to as QC lattice v, was patterned, which is related to the pattern used for QC lattices i–iv by a 36° rotation of the central decagon. A magnetic field was then applied *in-situ* in the TEM and images were recorded at field values around a hysteresis loop. The maximum field that was applied was ± 800 Gauss, but images were only visible over a field range of ± 200 Gauss. The magnetization direction in each bar was determined from the Fresnel contrast in an under-focus BF TEM image, rather than using magnetic induction maps obtained from TIE reconstructions²⁶.

References

- Castelnovo, C., Moessner, R. & Sondhi, S. L. Magnetic Monopoles in Spin Ice. *Nature* **451**, 42–45 (2008).
- Harris, M., Bramwell, S., McMorrow, D., Zeiske, T. & Godfrey, K. Geometrical frustration in the ferromagnetic pyrochlore $\text{Ho}_2\text{Ti}_2\text{O}_7$. *Phys. Rev. Lett.* **79**, 2554–2557 (1997).
- Snyder, J. *et al.* Low temperature spin freezing in the $\text{Dy}_2\text{Ti}_2\text{O}_7$ spin ice. *Phys. Rev. B* **69**, 064414 (2004).
- Heyderman, L. J. & Stamps, R. L. Artificial ferroic systems: novel functionality from structure, interactions and dynamics. *J. Phys.: Condensed Matter* **25**, 363201 (2013).
- Budrikis, Z. Disorder, edge and field protocol effects in athermal dynamics of artificial spin ice. In *Solid Shyicstate P* (ed. Camley, R. E. & Stamps, R. L.) 109–236 (Elsevier, 2014).
- Mengotti, E. *et al.* Real space observation of emergent magnetic monopoles and associated Dirac strings in artificial kagome spin ice. *Nat. Phys.* **7**, 68–74 (2010).
- Morgan, J. P., Stein, A., Langridge, S. & Marrows, C. H. Thermal ground-state ordering and elementary excitations in artificial magnetic square ice. *Nat. Phys.* **7**, 75–79 (2011).
- Ladak, S., Read, D. E., Perkins, G. K., Cohen, L. F. & Branford, W. R. Direct observation of magnetic monopole defects in an artificial spin-ice system. *Nat. Phys.* **6**, 359–363 (2010).
- Tamura, R., Muro, Y., Hiroto, T., Nishimoto, K. & Takabatake, T. Long range magnetic order in the quasicrystalline approximant Cd_6Tb . *Phys. Rev. B* **82**, 220201 (2010).
- Goldman, A. I. *et al.* A family of binary magnetic icosahedral quasicrystals based on rare earths and cadmium. *Nat. Mater.* **12**, 714–718 (2013).
- Vedmedenko, E. Y., Oepen, H. P. & Kirschner, J. Decagonal quasiferromagnetic microstructure on the Penrose tiling. *Phys. Rev. Lett.* **90**, 137203 (2003).
- Jagannathan, A., Motz, B. & Vedmedenko, E. Novel properties of frustrated low-dimensional magnets with pentagonal symmetry. *Philos. Mag.* **91**, 2765–2772 (2011).
- Bhat, V. S. *et al.* Controlled magnetic reversal in permalloy films patterned into artificial quasicrystals. *Phys. Rev. Lett.* **111**, 077201 (2013).
- Farmer, B. *et al.* Nonstochastic magnetic reversal in artificial quasicrystalline spin ice. *J. Appl. Phys.* **115**, 17E133 (2014).
- Bhat, V. S. *et al.* Ferromagnetic resonance study of eightfold artificial ferromagnetic quasicrystals. *J. Appl. Phys.* **115**, 17C502 (2014).
- Farmer, B. *et al.* Direct imaging of coexisting ordered and frustrated sublattices in artificial ferromagnetic quasicrystals. *Phys. Rev. B* **93**, 134428 (2016).
- Ke, X. *et al.* Energy minimization and ac demagnetization in a nanomagnet array. *Phys. Rev. Lett.* **101**, 037205 (2008).
- Donahue, M. J. & Porter, D. G. *The object oriented micromagnetic framework (OOMMF) project at ITL*. (2016) Available at: <http://math.nist.gov/oommf>. (Accessed :28th April, 2016).
- Phatak, C., Pan, M., Petford-Long, A. K., Hong, S. & De Graef, M. Magnetic interactions and reversal of artificial square spin ices. *New J. Phys.* **14**, 075028 (2012).
- Qi, Y., Brintlinger, T. & Cumings, J. Direct observation of the ice rule in an artificial kagome spin ice. *Phys. Rev. B* **77**, 094418 (2008).
- Ladak, S., Read, D., Tyliszczak, T., Branford, W. R. & Cohen, L. F. Monopole defects and magnetic Coulomb blockade. *New Journ. Phys.* **13**, 023023 (2011).
- Zhang, S., Petford-Long, A. K., Heinonen, O. & Phatak, C. Vortex jump behavior in coupled nanomagnetic heterostructures. *Appl. Phys. Lett.* **105**, 212409 (2014).
- Morgan, J. P. *et al.* Real and effective thermal equilibrium in artificial square spin ices. *Phys. Rev. B* **87**, 024405 (2013).
- Zhang, S. *et al.* Crystallites of magnetic charges in artificial spin ice. *Nature* **500**, 553–557 (2013).
- Bhat, V. S. *et al.* Non-stochastic switching and emergence of magnetic vortices in artificial quasicrystal spin ice. *Physica C* **503**, 170–174 (2014).
- DeGraef, M. & Petford-Long, A. K. Lorentz Microscopy in *Characterization of Materials* (ed. Kaufmann, E. N.) 1787–1801 (John Wiley and Sons, 2012).
- Gureyev, T. E., Roberts, A. & Nugent, K. A. Partially coherent fields, the transport-of-intensity equation, and phase uniqueness. *J. Opt. Soc. Am.* **12**, 1942–1946 (1995).
- Phatak, C., Petford-Long, A. K., Heinonen, O., Tanase, M. & De Graef, M. Nanoscale structure of the magnetic induction at monopole defects in artificial spin-ice lattices. *Phys. Rev. B* **83**, 174431 (2011).

Acknowledgements

This work was supported by the US Department of Energy, Office of Science, Basic Energy Sciences, Materials Sciences and Engineering Division. Use of the Center for Nanoscale Materials was supported by the US

Department of Energy, Office of Science, Office of Basic Energy Sciences, under contract no. DE-AC02-06CH11357. We acknowledge J. Pearson for help with thin film deposition.

Author Contributions

V.B. prepared the samples, recorded the images and performed the image reconstructions, V.B. and C.P. performed micromagnetic simulations, V.B., F.B., C.P. and A.K.P.-L. wrote the main manuscript and prepared Figures 1–5. All authors contributed to analysis of the data and reviewed the manuscript

Additional Information

Competing financial interests: The authors declare no competing financial interests.

How to cite this article: Brajuskovic, V. *et al.* Real-space observation of magnetic excitations and avalanche behavior in artificial quasicrystal lattices. *Sci. Rep.* **6**, 34384; doi: 10.1038/srep34384 (2016).



This work is licensed under a Creative Commons Attribution-NonCommercial-NoDerivs 4.0 International License. The images or other third party material in this article are included in the article's Creative Commons license, unless indicated otherwise in the credit line; if the material is not included under the Creative Commons license, users will need to obtain permission from the license holder to reproduce the material. To view a copy of this license, visit <http://creativecommons.org/licenses/by-nc-nd/4.0/>

© The Author(s) 2016